




Article

Feasibility of Ultra-Wideband Channels at Millimeter Wavelengths Faded by Rain in GeoSurf Satellite Constellations

Emilio Matricciani ^{*}, Maurizio Magarini  and Carlo Riva 

Dipartimento di Elettronica, Bioingegneria e Informazione, Politecnico di Milano, 20133 Milan, Italy; maurizio.magarini@polimi.it (M.M.); carlo.riva@polimi.it (C.R.)

* Correspondence: emilio.matricciani@polimi.it

Abstract: We have studied the interference caused by amplitude and phase distortions induced by rain in ultra-wideband communication systems designed for using amplitude modulation in GeoSurf future satellite constellations. The results concern radio links simulated with the synthetic storm technique at Spino d'Adda (Italy), Madrid (Spain) and Tampa (Florida), which are sites located in different climatic regions. The conclusions are (a) the three sites, although in different climatic zones, are practically indistinguishable; (b) the channel signal-to-noise ratio can be increased or decreased by interference with equal probability. Channel theoretical capacity loss, even in the worst case, is very limited and rain, therefore, does not cause significant linear distortions in ultra-wideband channels at millimeter waves; therefore, these channels could be used at millimeter waves.

Keywords: baseband channel; GeoSurf constellations; interference; linear distortions; millimeter wavelengths; passband channel; rain attenuation; synthetic storm technique; time delay; ultra-wideband channels



Citation: Matricciani, E.; Magarini, M.; Riva, C. Feasibility of Ultra-Wideband Channels at Millimeter Wavelengths Faded by Rain in GeoSurf Satellite Constellations. *Telecom* **2023**, *4*, 732–745. <https://doi.org/10.3390/telecom4040033>

Academic Editor: Petros Bithas

Received: 17 July 2023

Revised: 18 September 2023

Accepted: 10 October 2023

Published: 25 October 2023



Copyright: © 2023 by the authors. Licensee MDPI, Basel, Switzerland. This article is an open access article distributed under the terms and conditions of the Creative Commons Attribution (CC BY) license (<https://creativecommons.org/licenses/by/4.0/>).

1. Satellite Constellations with Zenith Propagation Paths at Any Site

Among satellite constellations, the GeoSurf constellations are a good choice for future worldwide internet infrastructure because they share most of the advantages of current GEO (geostationary), MEO (medium Earth orbit) and LEO (low Earth orbit) satellite constellations without suffering most of their drawbacks because they emulate the geostationary orbit with zenith paths in sites located at any latitude [1].

In [2], we have compared the tropospheric attenuation of GeoSurf zenith paths with the paths of GEO, MEO and LEO satellites.

In [3], we have assessed how the annual average probability distribution $P(A)$ of exceeding a given rain attenuation A (dB) depends on the carrier frequency f_c (GHz) in the GeoSurf paths at sites in different climatic regions. All these studies refer to narrow-band channels, i.e., channels with negligible linear (amplitude and phase) distortions.

In [4], we have estimated the slowly time-varying transfer function and linear distortions that are likely found in ultra-wideband radio links in GeoSurf constellations working at millimeter wavelengths. As a practical example, the bandwidth considered was 10 GHz wide, centered at 80 GHz (W-Band), because we think it might be used in future worldwide internet radio links using spread spectrum modulation and code division multiple access (CDMA) [5–10] with BPSK and QPSK modulation, once high-frequency large wideband technology—now developed at lower frequencies [11]—will also be available at W-band. CDMA can provide a large processing gain and can be designed without considering issues related to frequency and access coordination which, together with the advantages of the GeoSurf constellations mentioned in Reference [1], can be an effective choice to provide high bit rates to users.

The literature on what today is defined as “wideband” communication does not refer to rain attenuation or to the ultra-wideband radio links studied here but instead refers only to radio links in clear-sky conditions (mainly multipath), both for terrestrial and satellite

systems [5,12–16]; therefore, we discuss these topics further, following work carried out by [4,17].

Following our previous study [4], the purpose of this paper is to assess—with simulations using onsite rain rate time series and the synthetic storm technique (SST) [18]—the interference due to amplitude and phase distortions produced by rain attenuation in the ultra-wideband communication systems mentioned above and designed for using double sideband-suppressed carrier (DSB-SC) modulation in both quadrature channels (QPSK). We assume that the total signal-to-noise ratio (SNR) of the Gaussian channel is greater than the minimum required to guarantee a bit error probability smaller than the maximum value tolerated by users. Under this hypothesis, we estimate how the in-band attenuation and phase delay affect the baseband digital signal. We evaluate the sampler output of a direct channel (e.g., the cosine channel, inter-symbol interference, ISI) and the quadrature interference (QI) coming from the orthogonal channel (the sine channel, referred to also as the quadrature channel).

For illustrating the characteristics of the interference, we report the results concerning radio links simulated at Spino d’Adda (Italy), Madrid (Spain) and Tampa (Florida), which are sites in different climatic regions (Table 1). We have considered these specific sites because the rain rate time series $R(t)$ (mm/h)—averaged in 1 min intervals—have been continuously recorded onsite for several years, which is a sufficiently long period to provide reliable experimental results when SST is applied.

The rain fade in GeoSurf radio links is independent of the particular GeoSurf design (e.g., altitude and number of satellites) because all paths to/from a satellite of the constellation are always locally vertical (zenith). To determine the slowly time-varying passband and baseband equivalent transfer functions distorted by rain, we must know the rain attenuation $A(t)$ (dB) and the phase delay $\Phi(t)$ (degrees) time series. Both are calculated with the SST as shown in [4,18].

After this introduction, Section 2 shows examples of the results obtained with the SST; Section 3 recalls how to calculate passband and baseband transfer functions; Section 4 reports histograms of interference; Section 5 models probability distributions of interference; Section 6 calculates the theoretical channel capacity loss; Section 7 reports a general conclusion and indicates future work.

Table 1. Geographical coordinates, altitude (km), rain height H_R (km), number of years of continuous rain rate time series measurements at the indicated sites.

Site	Latitude N (°)	Longitude E (°)	Altitude H_S (km)	Precipitation Height H_R (km)	Rain Rate Data Bank (Years)
Spino d’Adda (Italy)	45.4	9.5	0.084	3.341	8
Madrid (Spain)	40.4	356.3	0.630	3.001	8
Tampa (Florida)	28.1	277.6	0.050	4.528	4

2. Rain Attenuation and Phase Delay Due to Rain in Zenith Propagation Paths

To calculate the complex passband (radio frequency) and complex baseband equivalent transfer functions of direct and orthogonal channels in DSB-SC modulation, defined and discussed in [4] and based on classical linear modulation theory (e.g., [19,20]), we must know the time series $A(t)$ (dB) and $\Phi(t)$ (degrees). Both are calculated with the SST [18], as shown in [4], with the modelling of [21–23].

Figure 1 shows the average annual probability distribution $P(R)$ of exceeding R (mm/h, averaged in 1 min) measured at Spino d’Adda, Madrid and Tampa. The different climatic rain conditions at these sites are clearly evident if the rain rates exceeded at equal probability are compared.

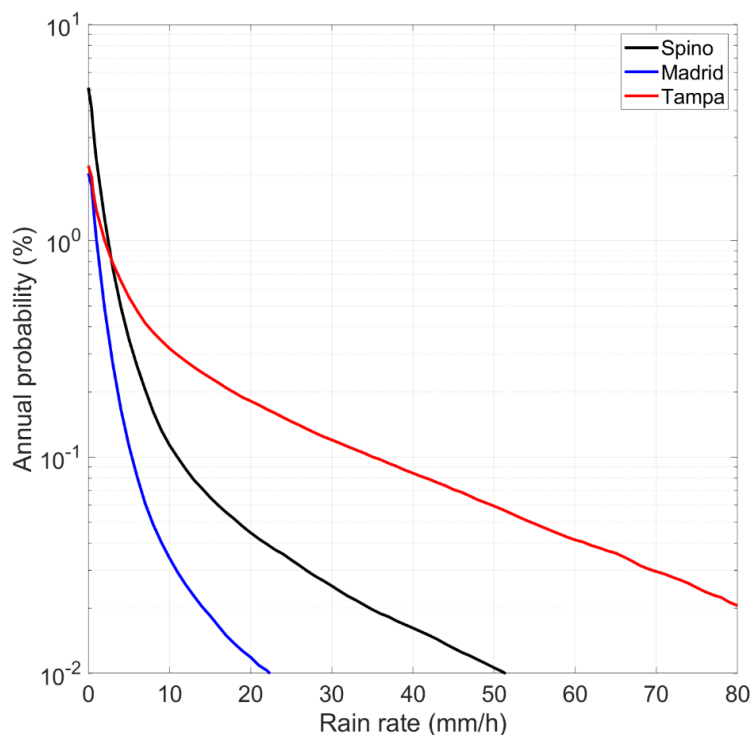


Figure 1. Annual probability distribution (%) $P(R)$ of exceeding the value indicated in abscissa at Spino d'Adda, Madrid and Tampa.

Figure 2a shows the annual probability distribution $P(A)$ of exceeding A (dB) calculated with Equation (8) of Reference [4], and Figure 2b shows the corresponding annual probability distribution $P(\Phi)$ of exceeding Φ (degrees) calculated with Equation (9) of Reference [4].

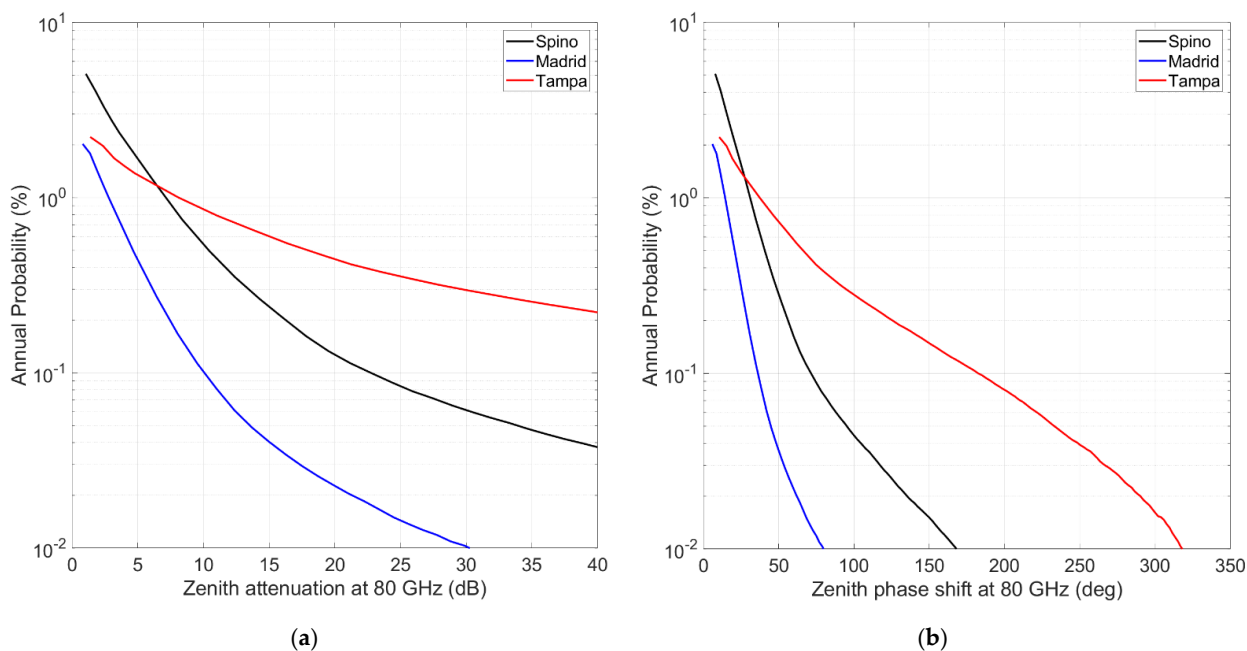


Figure 2. (a) Annual probability distribution (%) $P(A)$ of exceeding the value indicated in abscissa at Spino d'Adda, Madrid and Tampa; (b) annual probability distribution (%) $P(\Phi)$ of exceeding the value indicated in abscissa at Spino d'Adda, Madrid and Tampa, at 80 GHz and with circular polarization.

In the following, we consider the relative phase delay (degrees) at radio frequency ψ :

$$\varphi(\psi) = \Phi(\psi) - \Phi(\psi = f_c) \quad (1)$$

We defined the time delay (picoseconds):

$$T(t) = \frac{1000}{360\psi} \Phi(t) \quad (2)$$

where ψ is measured in GHz and the relative time delay is given by

$$\tau(f) = T(\psi) - T(\psi = f_c) \quad (3)$$

We defined the normalized magnitude $|H(\psi)|$ of the passband transfer function $H(\psi)$, at time t , as

$$|H(\psi)| = 10^{\frac{A(f_c) - A(\psi)}{20}} \quad (4)$$

The real and imaginary parts of $H(\psi)$ are given by

$$H_r(\psi) = |H(\psi)| \cos(\varphi(\psi)) \quad (5)$$

$$H_i(\psi) = |H(\psi)| \sin(\varphi(\psi))$$

From Equation (5), according to Reference [4] (see Equations (5)–(7) of [4]), we obtain the equivalent baseband complex transfer function of the direct channel as

$$H_{ed}(f) = H_{edr}(f) + jH_{edi}(f) \quad (6)$$

and the equivalent baseband complex transfer function that couples it to the orthogonal channel:

$$H_{eq}(f) = H_{eqr}(f) + jH_{eqi}(f) \quad (7)$$

Now, from $A(t)$ and $\Phi(t)$, the transfer function can be calculated at any time t , as we will recall in Section 3. Notice that, since $R(t)$ is averaged in 1 min, $A(t)$ and $\Phi(t)$ are also “averaged” in 1 min, so that the time-varying transfer function changes every minute and, therefore, very slowly compared to any digital signal so that, in every minute, the Gaussian channel is affected by the same in-band rain attenuation and phase delay (see [4]).

Moreover, we assume that at any time t , the channel SNR is larger than the minimum required by the bit error probability constraint; therefore, the rain fade, in order to be compensated with power control or with other techniques, is that which is measured at the highest frequency of the upper side-band, i.e., at 85 GHz in our exercise. Because our purpose is to study transfer functions, we assume the channel is still working as required; in other words, outages are not considered as they are not directly related to transfer functions.

An example illustrates how the SST transforms $R(t)$ into $A(t)$ and $T(t)$. Figure 3 shows $R(t)$ recorded in Tampa and Figures 4 and 5 show the corresponding $A(t)$ and the time delay $T(t)$ at 80 GHz and the relative values at the extremes of the 10 GHz bandwidth centered at 80 GHz. Notice that since $A(t)$ and $T(t)$ increase with frequency non-linearly in decibels and in picoseconds, the relative differences are not odd functions.

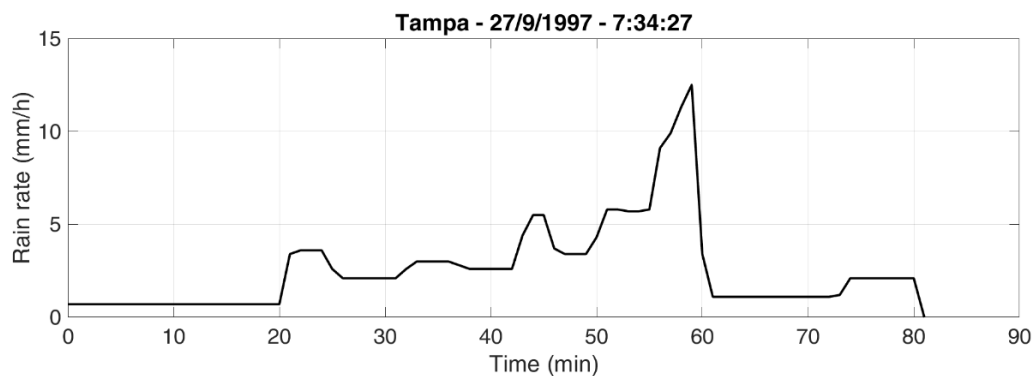


Figure 3. Rain rate time series $R(t)$ recorded at Tampa on 27 September 1997. According to the rain gauge collecting rainfall, the rain event started at 7:34:27 AM, local time. Samples are averaged in 1 min.

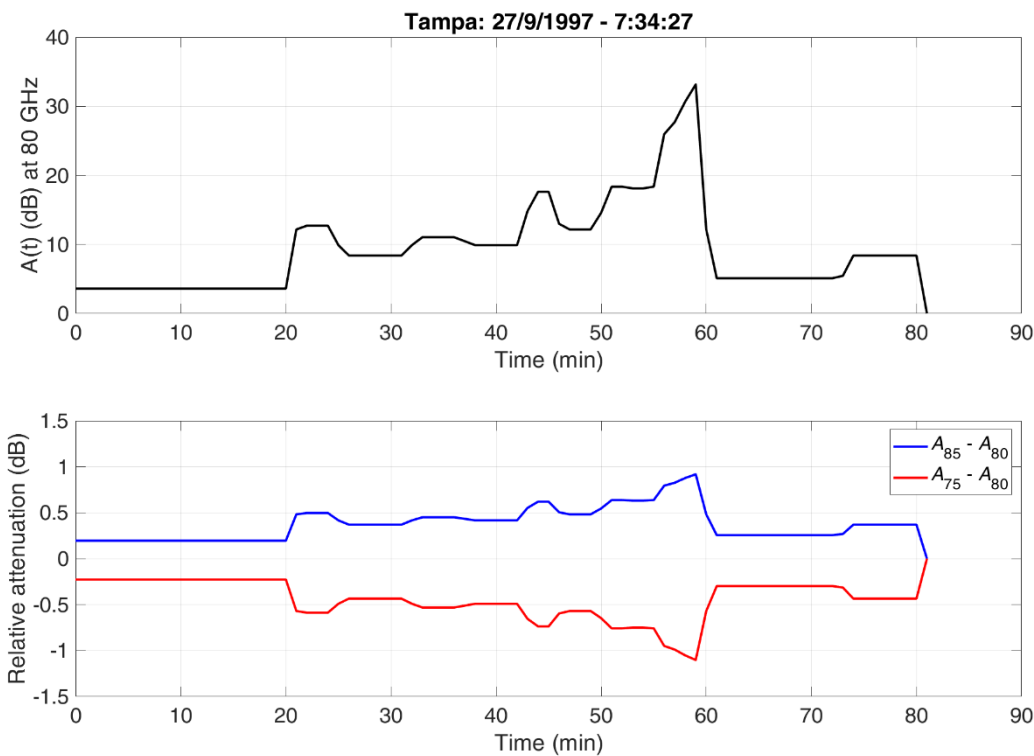


Figure 4. SST simulated event at Tampa, 27 September 1997, started at 7:34:27 AM local time. **(Upper panel):** rain attenuation $A(t)$ (dB) at 80 GHz (circular polarization). **(Lower panel):** relative attenuation at the extremes of a 10 GHz bandwidth. Sampling time is 1 min.

From these time series, we can calculate the passband and equivalent baseband transfer functions, according to the theory discussed in [4].

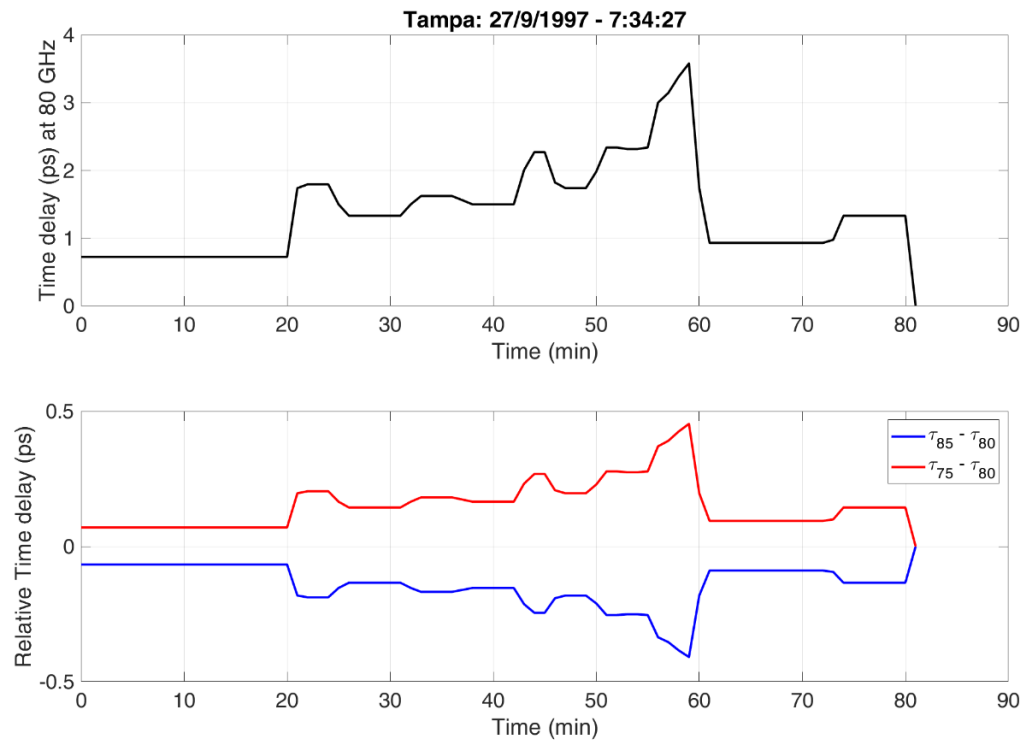


Figure 5. SST simulated event at Tampa, 27 September 1997, started at 7:34:27 AM, local time. (**Upper panel**): phase delay $T(t)$ (picoseconds) at 80 GHz (circular polarization). (**Lower panel**): relative phase delay at the extremes of a 10 GHz bandwidth. Sampling time is 1 min.

3. Ultra-Wideband Channels Distorted by Rain

In this section, we recall the theoretical flowchart of the digital receivers. Figures 6 and 7 show the baseband receiver in ideal conditions and in rain conditions. $S(f)$ is the two-sided spectrum of the Nyquist pulse, $\sqrt{S(f)}$ is the matched filter, $n(t)$ is the receiver total additive Gaussian white noise.

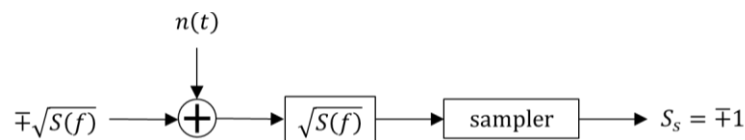


Figure 6. Flowchart of the baseband receiver in ideal conditions. $S(f)$ is the two-sided spectrum of the Nyquist pulse, $\sqrt{S(f)}$ is its matched filter, $n(t)$ is the receiver total additive Gaussian white noise.

In the ideal case (Figure 6), the amplitude at the sampling time is normalized to unity. In other words, a hard decision gives ∓ 1 by sampling the pulse peak at the sampling time $t = 0$.

In the rain fade case (Figure 7), we suppose that, at any time t , the received signal is amplified by multiplying it by $10^{\frac{A(f_c)}{20}}$ to remove the variable rain attenuation at the carrier frequency $f_c = 80$ GHz (this is not related to the outage condition discussed above, which must consider the rain attenuation at 85 GHz). After this multiplication, only the in-band signal variations of the carrier frequency are left, which is the effect we want to study. At the output of the sampler, before the hard decision, we find the algebraic sum $s_{sd} + s_{sq}$ of direct and orthogonal channel samples at the reference time $t = 0$, corresponding to the peak value of the direct (cosine) and orthogonal channel (sine) pulses present simultaneously in the two orthogonal channels. In general, however, both values are affected by self-channel (ISI) interference due to the tails of the previous and following pulses and to the interference coming from the orthogonal channel (QI).

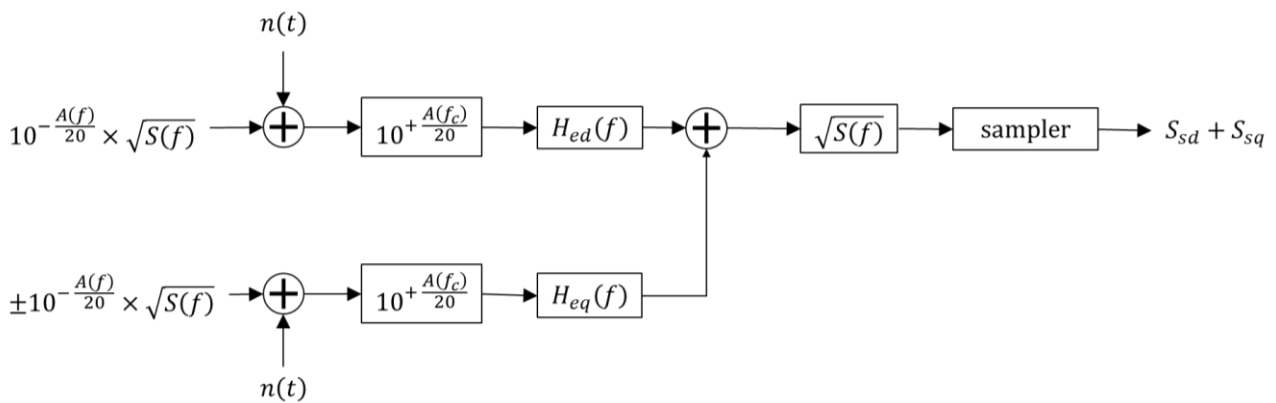


Figure 7. Flowchart of the quadrature baseband receiver in rain attenuation. $S(f)$ is the two-sided spectrum of the Nyquist reference pulse assumed to be positive, $\sqrt{S(f)}$ is the matched filter and $n(t)$ is the receiver total additive Gaussian white noise for each channel of equal power.

From these equations, as shown in [4], we can calculate the baseband equivalent transfer functions at frequency f , with $H_{ed}(f)$ for the direct channel and $H_{eq}(f)$ for the orthogonal channel (Figure 7), whose averages for Spino d’Adda, Madrid and Tampa are reported in [4].

In the next section, we report the statistics of interference due to the direct channel (ISI) and to the quadrature channel (QI). These results are fundamental for assessing the feasibility of the ultra-wideband radio link.

4. Experimental Interference

Numerical results have been obtained by means of time-domain simulations of the system described in Figure 7 in MATLAB/Simulink®. We have simulated the transmission of a sequence of 10^4 symbols drawn from a quadrature phase-shift keying (QPSK) modulation of long sequences of independent bits at the bit rate ρ (bits per second, bps) according to the value of the roll-off factor r . Since the baseband width is fixed to $B = 5$ GHz, the bit rate is a function of r , given by

$$\rho = \frac{2B}{1+r} \tag{8}$$

We have simulated bit rates corresponding to $r = 0.25$, i.e., $\rho = 8$ Gbps (gigabits per second); $r = 0.50$, $\rho = 6.67$ Gbps; $r = 1$, $\rho = 5$ Gbps. A numerical approximation of the continuous-time square-root Nyquist filter $\sqrt{S(f)}$ has been implemented by considering a windowing of 16 symbol intervals and an oversampling factor of 4 compared to the symbol rate.

Because we refer to normalized values, the algebraic sum of total interference $s_{sd} + s_{sq}$ gives the factor by which the SNR Γ obtainable in the ideal channel (Figure 6) must be multiplied to obtain the SNR in the presence of ISI and QI. Therefore, we defined the channel factor μ :

$$\mu = s_{sd} + s_{sq} \tag{9}$$

The SNR obtainable with interference is given by

$$\gamma = \mu^2 \Gamma \tag{10}$$

$$\gamma(\text{dB}) = 10 \times \log_{10} \mu^2 + 10 \times \log_{10} \Gamma$$

In applying these equations, we assume that the channel Gaussian noise power is constant, although it should slightly increase with rain attenuation.

Our main results are the histograms (relative frequency) of the sampler output amplitude (dB) first but only with ISI and then only with ISI and QI, i.e., with the total interference. To show the dependence on the rain attenuation calculated at the center frequency (i.e.,

80 GHz), we have considered the cases in which rain attenuation (and corresponding time delay) was in the following ranges: $9 \leq A_{80 \text{ GHz}} \leq 11 \text{ dB}$ (referred to, for short, as “10” dB), $18 \leq A_{80 \text{ GHz}} \leq 22 \text{ dB}$ (“20” dB) and $27 \leq A_{80 \text{ GHz}} \leq 33 \text{ dB}$ (“30” dB).

Figure 8 shows the relative frequency histogram of the channel factor μ (dB) for $r = 0.25$, Figure 9 for $r = 0.50$ and Figure 10 with $r = 1$.

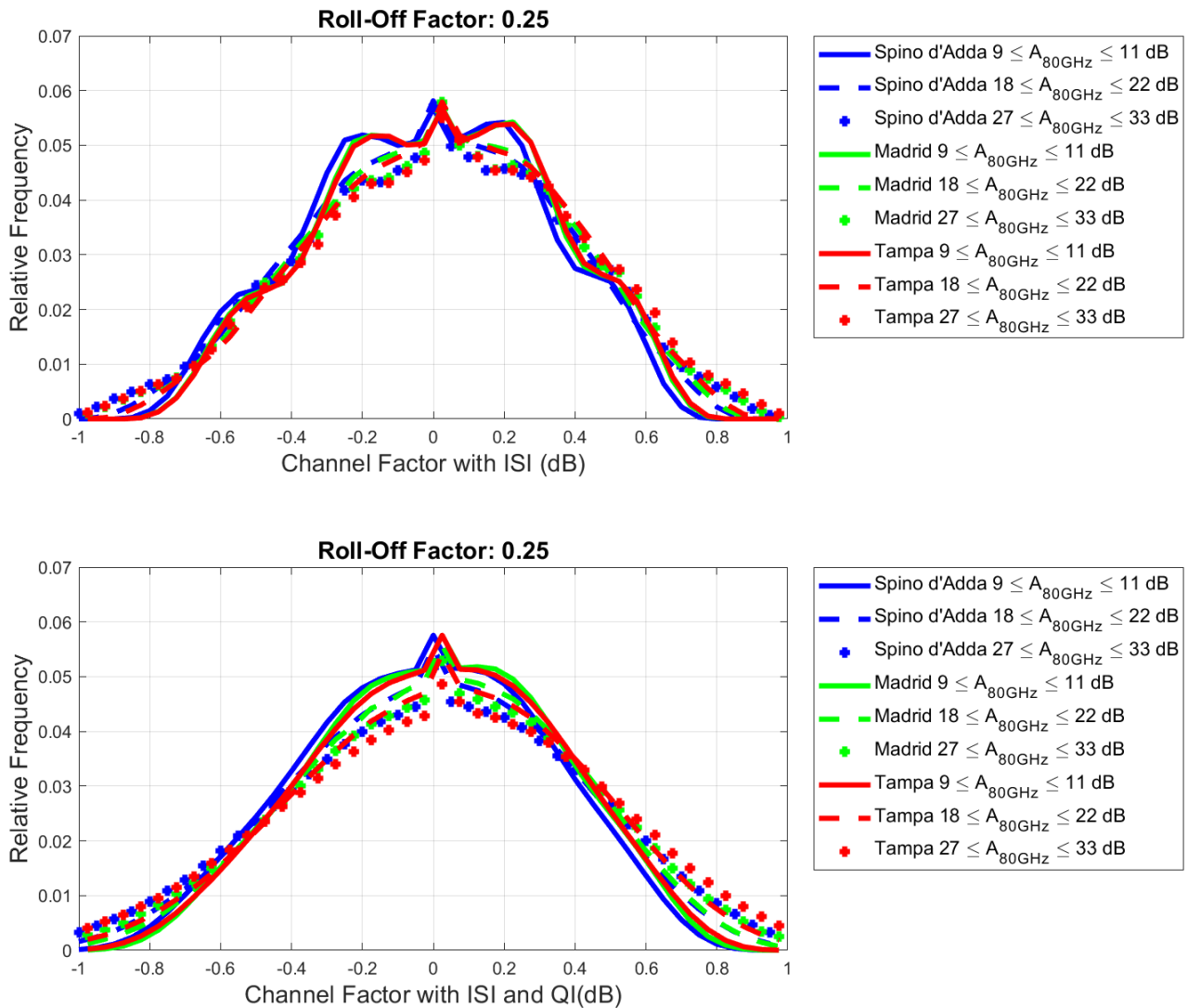


Figure 8. Relative frequency histogram of the channel factor μ (dB) with ISI (**upper panel**) and with ISI and QI (**lower panel**). **Color key:** blue = Spino d’Adda; green = Madrid; red = Tampa. **Curve key:** continuous $9 \leq A_{80 \text{ GHz}} \leq 11 \text{ dB}$; dashed $18 \leq A_{80 \text{ GHz}} \leq 22 \text{ dB}$; “+” $27 \leq A_{80 \text{ GHz}} \leq 33 \text{ dB}$. Roll-off factor $r = 0.25$.

From these results, we can draw the following general conclusions:

- (1) The three sites, although in different climatic zones, are practically indistinguishable in all cases.
- (2) All histograms show even symmetry; therefore, indicating that for about 50% of the time, we can consider the channel factor to be either $\mu < 0$ (dB), therefore, $\gamma < \Gamma$; or $\mu > 0$ (dB), therefore, $\gamma > \Gamma$.
- (3) Histograms with only ISI and with ISI + QI are distinguishable.
- (4) With ISI only, the lowest range of attenuation (10 dB) shows more marked peaks at $\mu = 0$ dB and $\mu \approx \pm 0.3$ dB. These peaks are largely smoothed when QI is also added.

- (5) The roll-off factor r plays a small role because the values of the peaks change a little, especially for $r = 1$.

Because of these general findings, in Figure 11, we have drawn the average relative frequency histograms by distinguishing only the three attenuation ranges. In other words, this figure should provide a “global” frequency distribution of the channel factor in a 10 GHz bandwidth centered at 80 GHz. In the next section, we will propose a theoretical approach which can justify these findings.

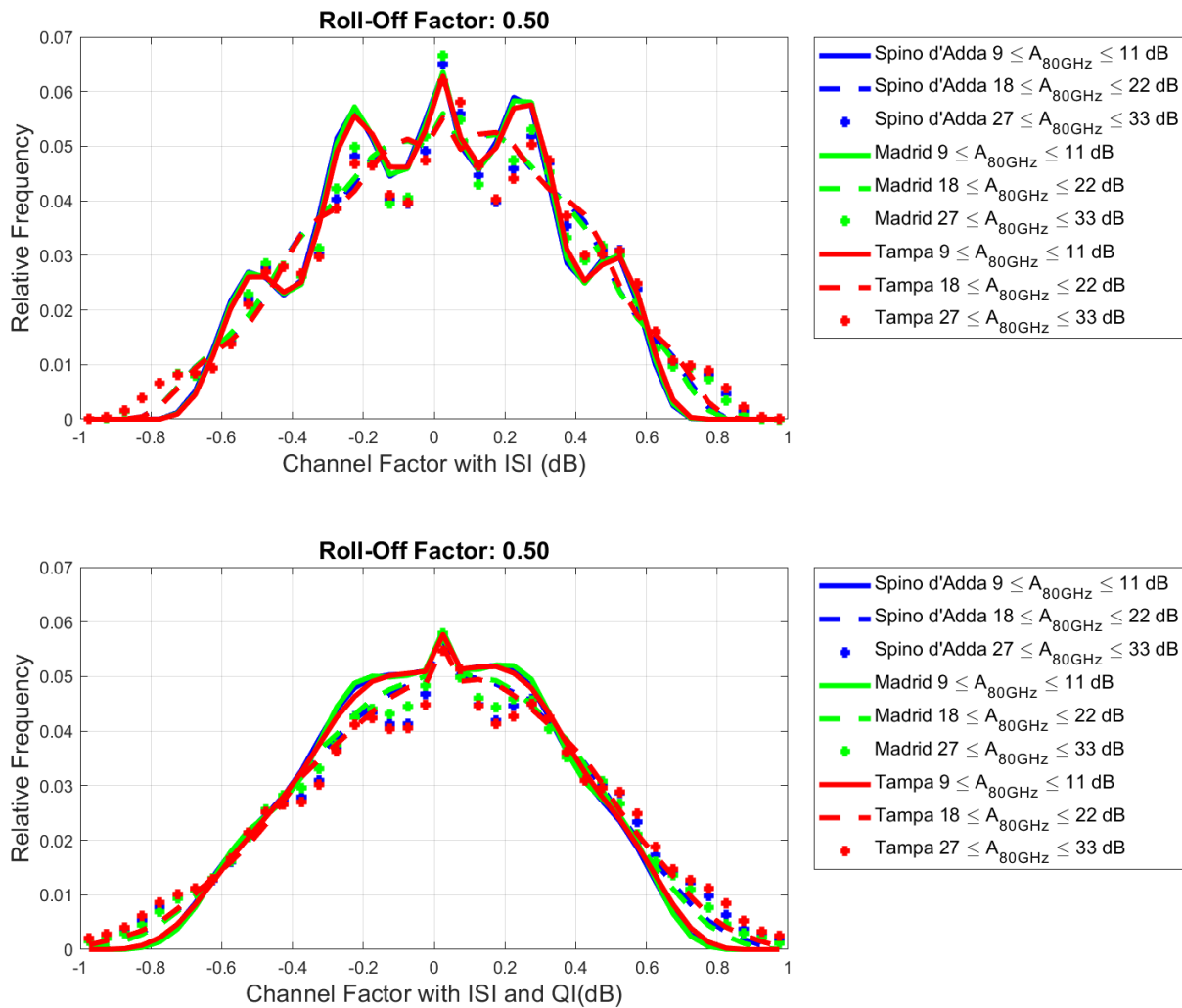


Figure 9. Relative frequency histogram of the channel factor μ (dB) with ISI (**upper panel**) and with ISI and QI (**lower panel**). **Color key:** blue = Spino d’Adda; green = Madrid; red = Tampa. **Curve key:** continuous $9 \leq A_{80\text{ GHz}} \leq 11$ dB; dashed $18 \leq A_{80\text{ GHz}} \leq 22$ dB; “+” $27 \leq A_{80\text{ GHz}} \leq 33$ dB. Roll-off factor $r = 0.50$.

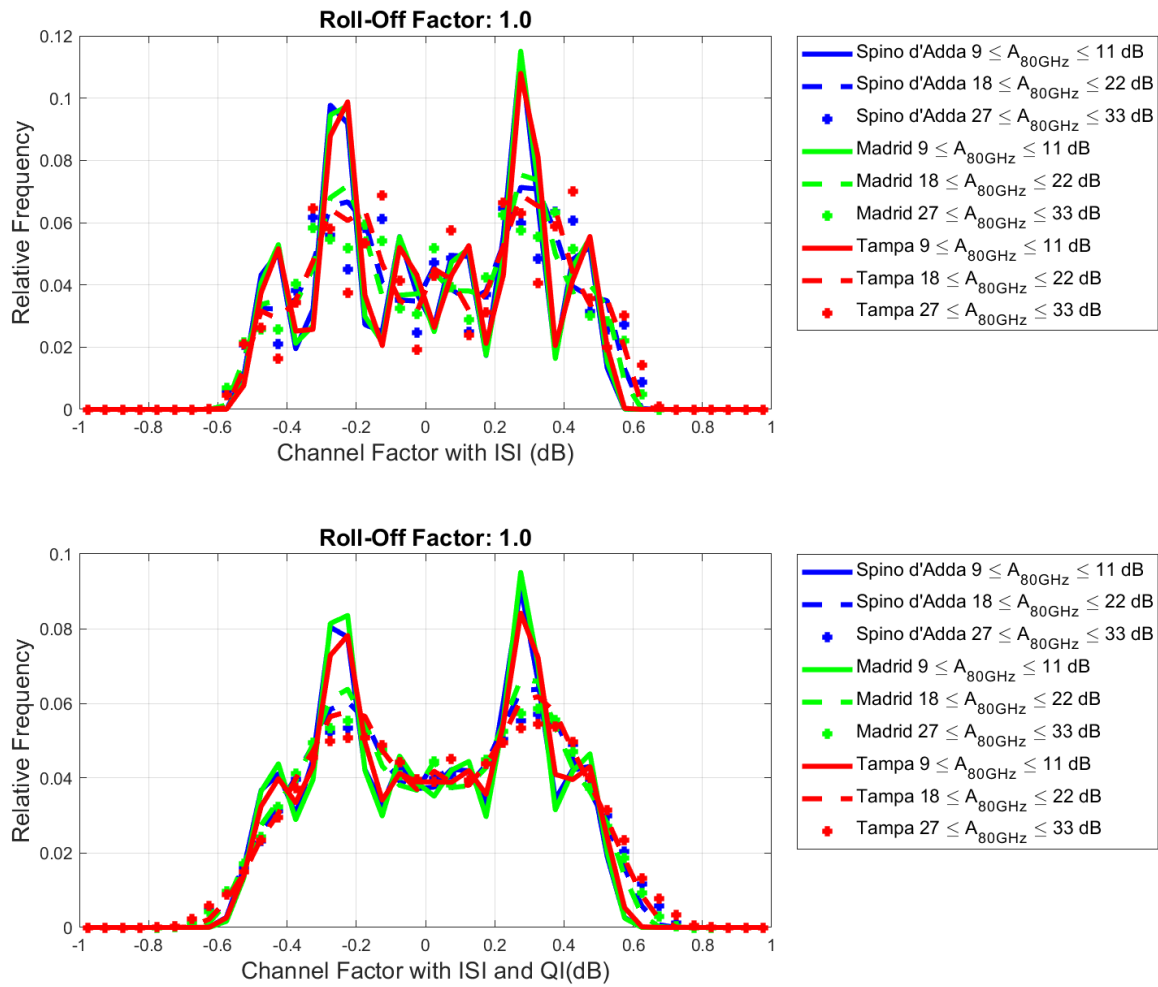


Figure 10. Relative frequency histogram of the channel factor μ (dB) with ISI (**upper panel**) and with ISI and QI (**lower panel**). **Color key:** blue = Spino d’Adda; green = Madrid; red = Tampa. **Curve key:** continuous $9 \leq A_{80\text{ GHz}} \leq 11$ dB; dashed $18 \leq A_{80\text{ GHz}} \leq 22$ dB; “+” $27 \leq A_{80\text{ GHz}} \leq 33$ dB. Roll-off factor $r = 1$.

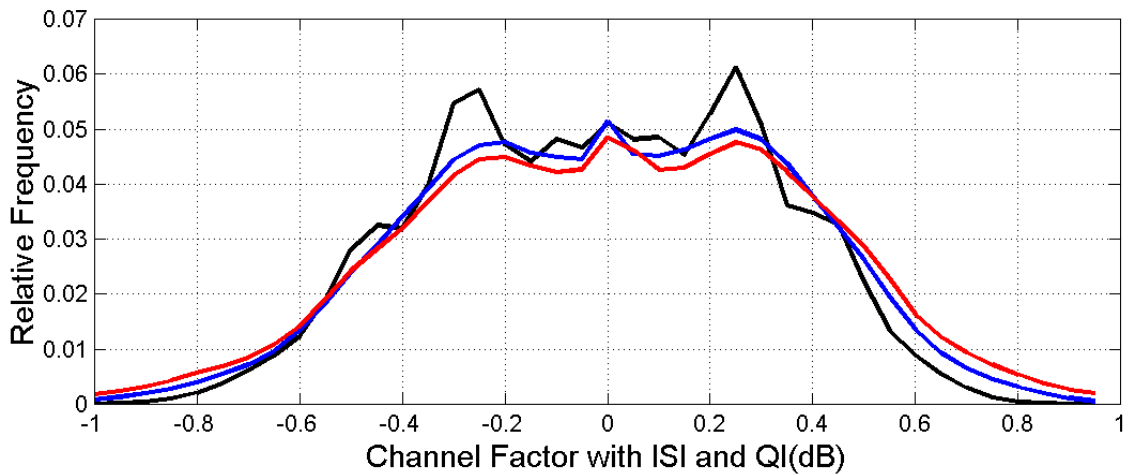


Figure 11. Average relative frequency histogram of the channel factor μ (dB) in the presence of ISI and QI. **Curve key:** black $9 \leq A_{80\text{ GHz}} \leq 11$; blue $18 \leq A_{80\text{ GHz}} \leq 22$; red $27 \leq A_{80\text{ GHz}} \leq 33$. Curves are averaged over the sites and roll-off factors.

5. Modeling Interference

In this section, we propose a theoretical approach which can justify the relative frequency histogram of the channel factor μ found in Section 4.

The channel factor μ at the sampling time t_k is given by

$$\begin{aligned}\mu(t_k = 0) &= \sum_{k=-N}^{k=+N} s_{sd}(t_k) + \sum_{k=-N}^{k=+N} s_{sq}(t_k) \\ \mu &= i_d + i_q\end{aligned}\quad (11)$$

Now, since both i_d and i_q are stochastic variables given by the sum of many independent values, their probability density function—according to the central limit theorem—should approach the Gaussian distribution; therefore, the probability density function of μ should be given by the convolution of two Gaussian models, i.e., another Gaussian probability distribution with a mean value given by the sum of the two mean values and variance given by the sum of the two variances; this hypothesis holds if all variables display the same order of magnitude [24,25].

Let us carry out some useful transformations. According to Figures 8–11, the channel factor μ ranges between -1 dB (i.e., $10^{-1/20} = 0.891$) and $+1$ dB ($10^{+1/20} = 1.122$). Now, by recalling that $\ln(x) \approx (x - 1)$ if $x \approx 1$, we can write

$$\mu \approx \ln(\mu) + 1 \quad (12)$$

Therefore, the relationship between μ in decibels and μ in linear units is given by:

$$\mu(\text{dB}) = \frac{10}{\ln(10)}(\mu - 1) \quad (13)$$

Hence, if μ is Gaussian, then $\mu(\text{dB})$ is also approximately Gaussian. However, Figures 8–10 seem to suggest two different overlapping Gaussian distributions, especially for $r = 1$. In other words, $\mu < 1$ and $\mu > 1$ seem due to two similar sets of data of equal variance but with mean values set approximately at about ± 0.3 dB; therefore, the central limit theorem applies to these two separate distributions. The overall relative frequency histograms shown in Figure 11 confirm this general finding, especially at low fade (~ 10 dB). The peak at about $\mu = 0$ dB can be explained by the Dirac pulse produced by the constant $-\frac{10}{\ln(10)}$ of Equation (13). In the experimental histograms, it is due to the very small spread of the sampler output amplitude due only to the reference pulse and not to the ISI or QI.

Now, the question is: how “bad” is the ultra-wideband channel discussed above? In the next section, we attempt a quantitative analysis by using Shannon’s channel capacity.

6. Channel Capacity Loss

In this section, we discuss a quantitative analysis of the results obtained in the ultra-wideband channels studied in the previous sections by using Shannon’s channel capacity. For this purpose, let us define the capacity factor c , independent of the roll-factor and the logarithm used in its definition, which is given by

$$c = \frac{\ln(1 + \mu^2 \Gamma)}{\ln(1 + \Gamma)} \quad (14)$$

In Figure 12, we show c versus Γ (dB), calculated at the extreme values of μ , and which namely approximately ± 1 dB.

Let us discuss only the worst case: the red curve referring to the negative values of μ (dB). We can notice that, as the signal-to-noise ratio Γ (dB) increases in ideal conditions (no rain), the capacity factor increases from $c = 0.825$ at $\Gamma = 3$ dB to $c = 0.950$ at $\Gamma = 20$ dB; therefore, the capacity loss ranges from 17.5% to 5%.

In conclusion, we think that the capacity loss in the worst case is very limited and that rain, therefore, does not cause significant linear distortions in ultra-wideband channels at millimeter waves.

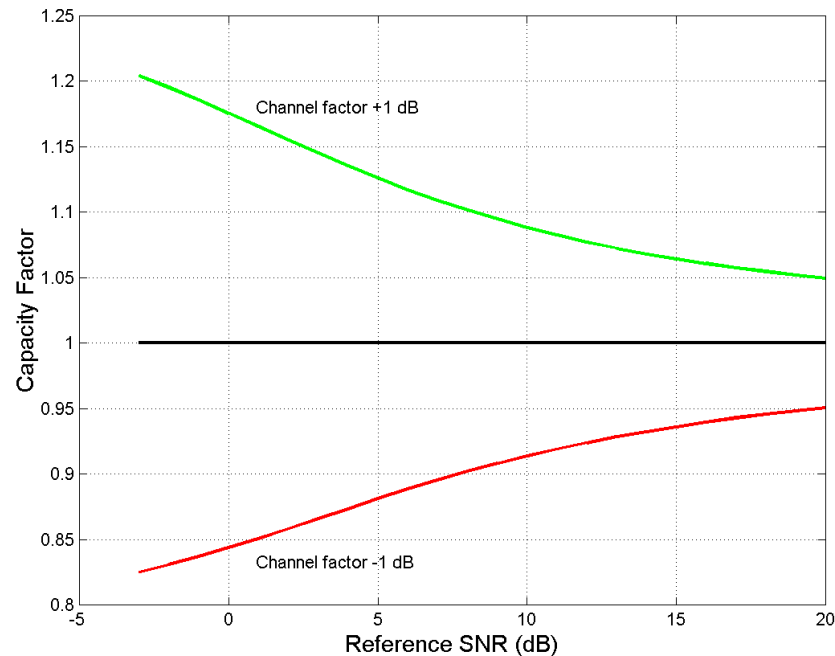


Figure 12. Capacity factor versus Γ (dB) at the extreme values of μ ; namely, ± 1 dB. The experimental values of Figures 10–12 are within these bounds.

7. Conclusions

Following our previous studies concerning GeoSurf satellite constellations, in the present paper, we have studied the interference due to amplitude and phase distortions produced by rain in ultra-wideband communication systems designed for using double sideband-suppressed carrier (DSB-SC) modulation.

For illustrating the general characteristics of linear interference due to rain in ultra-wideband channels, we have reported and discussed the results concerning radio links simulated with SST at Spino d'Adda (Italy), Madrid (Spain) and Tampa (Florida), which are sites located in different climatic regions. Numerical results have been obtained by means of time-domain simulations of the system.

After reviewing the classical theory of passband (radio frequency) and baseband equivalent transfer functions of direct and orthogonal channels in DSB-SC modulation, we have calculated them when radio links are faded by rain.

We defined the self-channel (ISI) interference due to the tails of the previous and following pulses and the interference coming from the orthogonal channel (QI). We have reached the following general conclusions:

- (1) The three sites considered, although in different climatic zones, are practically indistinguishable in all cases.
- (2) The channel factor μ can be either $\mu < 0$ (dB), therefore, $\gamma < \Gamma$; or $\mu > 0$ (dB), therefore, $\gamma > \Gamma$ with equal probability.
- (3) Histograms with only ISI or with ISI + QI are diverse.
- (4) With ISI only, the lowest range of attenuation (10 dB) shows more marked peaks in the relative frequency histograms at $\mu = 0$ dB and $\mu \approx \pm 0.3$ dB. These peaks are largely smoothed when QI is added.
- (5) The roll-off factor r plays a small role because the peaks change only for $r = 1$.

We have proposed a theoretical approach which can justify these findings.

In conclusion, the channel theoretical capacity loss, even in the worst case, is very limited and rain, therefore, does not cause significant linear distortions in ultra-wideband channels at millimeter waves in QPSK schemes.

Future work should be conducted in simulating higher-order QAM ultra-wideband channels to assess whether these channels are also affected a little by linear distortions due to rain.

Author Contributions: Conceptualization, E.M., M.M. and C.R.; methodology, E.M., M.M. and C.R.; software, E.M., M.M. and C.R.; investigation, E.M., M.M. and C.R.; data curation, E.M., M.M. and C.R.; writing—original draft preparation, E.M., M.M. and C.R.; writing—review and editing, E.M., M.M. and C.R.; visualization, E.M., M.M. and C.R. All authors have read and agreed to the published version of the manuscript.

Funding: This research received no external funding.

Data Availability Statement: Not applicable.

Acknowledgments: We wish to thank Roberto Acosta, at NASA years ago, for providing the rain rate data of Tampa and we also wish to thank José Manuel Riera, at the Universidad Politécnica de Madrid, for providing the rain rate data of Madrid.

Conflicts of Interest: The authors declare no conflict of interest.

References

1. Matricciani, E. Geocentric Spherical Surfaces Emulating the Geostationary Orbit at Any Latitude with Zenith Links. *Future Internet* **2020**, *12*, 16. [[CrossRef](#)]
2. Matricciani, E.; Riva, C.; Luini, L. Tropospheric Attenuation in GeoSurf Satellite Constellations. *Remote Sens.* **2021**, *13*, 5180. [[CrossRef](#)]
3. Matricciani, E.; Riva, C. Outage Probability versus Carrier Frequency in GeoSurf Satellite Constellations with Radio-Links Faded by Rain. *Telecom* **2022**, *3*, 504–513. [[CrossRef](#)]
4. Matricciani, E.; Riva, C. Transfer-functions and Linear Distortions in Ultra-Wideband Channels Faded by Rain in GeoSurf Satellite Constellations. *Future Internet* **2023**, *15*, 27. [[CrossRef](#)]
5. Kennedy, R.S. *Fading Dispersive Communication Channels*; Wiley: New York, NY, USA, 1969.
6. Turin, G.L. Introduction to spread spectrum antimultipath techniques and their application to urban digital radio. *Proc. IEEE* **1980**, *68*, 328–353.
7. Pickholtz, R.; Schilling, D.; Milstein, L. Theory of spread-spectrum communications—A tutorial. *IEEE Trans. Commun.* **1982**, *30*, 855–884.
8. Viterbi, A.J. *CDMA Principles of Spread Spectrum Communications*; Addison-Wesley: Reading, MA, USA, 1995.
9. Dinan, E.H.; Jabbari, B. Spreading codes for direct sequence CDMA and wideband CDMA cellular networks. *IEEE Commun. Mag.* **1998**, *36*, 48–54. [[CrossRef](#)]
10. Veeravalli, V.V.; Mantravadi, A. The coding-spreading trade-off in CDMA systems. *IEEE Trans. Sel. Areas Commun.* **2002**, *20*, 396–408. [[CrossRef](#)]
11. Matsusaki, Y.; Masafumi, N.; Suzuki, Y.; Susumu, N.; Kamei, M.; Hashimoto, A.; Kimura, T.; Tanaka, S.; Ikeda, T. Development of a Wide-Band Modem for a 21-GHz Band Satellite Broadcasting System. In Proceedings of the 2014 IEEE Radio and Wireless Symposium (RWS), Newport Beach, CA, USA, 19–23 January 2014.
12. Parsons, D. *The Mobile Radio Propagation Channel*; Wiley: New York, NY, USA, 1994.
13. Simon, M.K.; Alouini, M.S. *Digital Communication over Fading Channels: A Unified Approach to Performance Analysis*; Wiley: New York, NY, USA, 2000.
14. Greenstein, L.G.; Andersen, J.B.; Bertoni, H.L.; Kozono, S.; Michelson, D.G. (Eds.) Special Issue on Channel and Propagation Modeling for Wireless Systems Design. *J. Sel. Areas Commun.* **2002**, *20*. [[CrossRef](#)]
15. Goldsmith, A. *Wireless Communications*; Cambridge University Press: Cambridge, NY, USA, 2005.
16. Pérez-Fontan, F.; Pastoriza-Santos, V.; Machado, F.; Poza, F.; Witternig, N.; Lesjak, R. A Wideband Satellite Maritime Channel Model Simulator. *IEEE Trans. Antennas Propag.* **2022**, *70*, 214–2127. [[CrossRef](#)]
17. Matricciani, E. A Relationship between Phase Delay and Attenuation Due to Rain and Its Applications to Satellite and Deep-Space Tracking. *IEEE Trans. Antennas Propag.* **2009**, *57*, 3602–3611. [[CrossRef](#)]
18. Matricciani, E. Physical-mathematical model of the dynamics of rain attenuation based on rain rate time series and a two-layer vertical structure of precipitation. *Radio Sci.* **1996**, *31*, 281–295. [[CrossRef](#)]
19. Schwartz, M. *Information, Transmission, Modulation and Noise*, 4th ed.; McGraw-Hill Int. Ed.: New York, NY, USA, 1990.
20. Carassa, F. *Comunicazioni Elettriche*; Bollati Boringhieri: Turin, Italy, 1978.
21. Matricciani, E. Rain attenuation predicted with a two-layer rain model. *Eur. Transactions Telecommun.* **1991**, *2*, 715–727. [[CrossRef](#)]

22. Recommendation ITU-R P.839-4. *Rain Height Model for Prediction Methods*; ITU: Geneva, Switzerland, 2013.
23. Maggiori, D. Computed transmission through rain in the 1–400 GHz frequency range for spherical and elliptical drops and any polarization. *Alta Frequenza*. **1981**, *50*, 262–273.
24. Papoulis, A. *Probability & Statistics*; Prentice Hall: Hoboken, NJ, USA, 1990.
25. Lindgren, B.W. *Statistical Theory*, 2nd ed.; MacMillan Company: New York, NY, USA, 1968.

Disclaimer/Publisher's Note: The statements, opinions and data contained in all publications are solely those of the individual author(s) and contributor(s) and not of MDPI and/or the editor(s). MDPI and/or the editor(s) disclaim responsibility for any injury to people or property resulting from any ideas, methods, instructions or products referred to in the content.